

The Ephemeris and Dipping Spectral Behavior of X1624–490

Alan P. Smale¹

Laboratory for High Energy Astrophysics, Code 662, NASA/Goddard Space Flight Center, Greenbelt, MD 20771

Michael J. Church, Monika Bałucińska-Church

School of Physics & Astronomy, University of Birmingham, Edgbaston, Birmingham B15 2TT, UK

ABSTRACT

We present striking results from *Rossi X-ray Timing Explorer (RXTE)* observations of the 21-hr low mass X-ray binary X1624–490, showing five complex dips in unprecedented detail. For the first time, dipping is detected up to 15 keV. Prominent flares are also observed in the light curves, limited to energies above \sim 8 keV. Spectra selected by intensity during dip episodes can be well fit with a two-component model consisting of a point-like blackbody from the neutron star and progressive covering of an extended Comptonized region, presumably an accretion disk corona (ADC), corrected for photons scattered into and out of the X-ray beam by an interstellar dust halo. We find that the outer regions of the absorber are highly ionized and that electron scattering is totally responsible for the X-ray attenuation during shallow dipping. The timescales of dip ingress and egress indicate that the envelope of material absorbing the ADC has smaller angular size than the ADC itself, and that the ADC is likely limited to a height-to-radius ratio of 10%, rather than being spherical in extent. In addition, we have analyzed \sim 4.5 yrs of *RXTE* All Sky Monitor (ASM) coverage to derive the first accurate orbital ephemeris for X1624–490, with phase zero (the time of dip centers) well-described by the relation $245\ 0088.63918(69) + N \times 0.869907(12)$ (JD).

Subject headings: accretion, accretion disks — scattering — stars: binaries: close — stars: circumstellar matter — stars: individual (X1624–490) — stars: neutron — interstellar medium: extinction — X-rays: stars

¹Also Universities Space Research Association.

1. Introduction

The study of X-ray dipping sources has played a critical role in the understanding and visualization of how a low mass X-ray binary (LMXB) might look to a nearby astronomical observer; it is generally accepted that the dips are due to occultations of the central source by a thickened region of the accretion disk rim where the gas stream from the companion impacts upon the outer disk. However, the dips themselves also provide a wealth of physical information not limited to their role in defining the system geometry. From their irregular, ragged appearance and cycle-to-cycle differences in width and depth we know that the disk structure is dynamic. Also, spectral fitting results show that dips are associated with, but cannot be completely described by, increases in absorption of $N_H \gtrsim 10^{23} \text{ cm}^{-2}$.

X1624–490 is one of the most unusual members of this class; its persistent emission is the brightest ($6 \times 10^{37} \text{ erg s}^{-1}$), its dip profiles seemingly the most erratic, and its 21-hr orbital period is the longest – ~ 5 – 25 times longer than other dipping sources, corresponding to a much greater stellar separation and a larger accretion disk radius. Dipping is deep, $\sim 75\%$ in the 1–10 keV band, and can at times reach a stable lower level (Watson et al. 1985; Church & Bałucińska-Church 1995) suggesting that one spectral component is entirely removed. The source also exhibits strong flaring in which the X-ray flux can increase by 30% or more over timescales of a few thousand seconds. In this regard, it may provide an interesting overlap between the dipping LMXBs, generally assumed to be atoll sources by virtue of their persistent emission level and noise characteristics, and the Z-track sources with their well-known flaring branches (e.g. Hasinger & van der Klis 1989).

The depth, duration, and spectral evolution in dipping vary considerably between members of the dipping class. An additional complication is the fact that several sources exhibit an unabsorbed component of the spectrum, e.g. XB1916–053 (Smale et al. 1988, 1992), XB0748–676 (Parmar et al. 1986) and XB1254–690 (Courvoisier et al. 1986). More recently, it has been demonstrated that a unified approach describes the dipping sources (Church & Bałucińska-Church 1995; Church et al. 1997, Bałucińska-Church et al. 1999). Their model consists of point-like blackbody emission from the neutron star, plus extended Comptonized emission from the Accretion Disk Corona

(ADC), and a “progressive covering” description of absorption. In this description, the absorber on the outer edge of the accretion disk (White & Swank 1982) moves progressively across the emission regions, so that at any stage of dipping, part of the Comptonized emission is absorbed and part is not, giving rise to the observed unabsorbed component. As a point source, the blackbody is rapidly absorbed once the envelope of the absorber reaches the neutron star.

In previous observations of X1624–490 with *EXOSAT* and *Ginga*, a blackbody plus bremsstrahlung model was used to parameterize the spectra (Jones & Watson 1989). Subsequently, Church & Bałucińska-Church (1995) showed that the light curve at energies >5 keV was dominated by flaring, which can strongly modify the spectrum and make the spectral investigation of dipping difficult. By selecting sections of non-dip and dip data without apparent flaring, the above two-component model was found to fit the data well, showing that in deep dipping the blackbody component was totally absorbed, and the Comptonized component relatively little absorbed. However, with only one non-dip and one deep dip spectrum it was not possible to determine the extent of absorption of the Comptonized component.

A more recent *BeppoSAX* observation revealed the dust scattered halo of the source demonstrated by Angelini et al. (1997). Modeling of the radial distribution of count rate in the MECS at a series of energies below 5 keV allowed an optical depth to dust scattering of 2.4 ± 0.4 at 1 keV to be derived, the data being consistent with a cross-section varying as E^{-2} (Bałucińska-Church et al. 2000a). Spectral models of non-dip and dip data included the effects of this interstellar dust scattering, and good fits were obtained with the above two-component model, in which the blackbody had temperature $kT = 1.31 \pm 0.07$ keV, and the Comptonized emission was approximated by a cut-off power law with photon index of $\Gamma = 2.0^{+0.5}_{-0.7}$ and cut-off energy ~ 12 keV. While more sensitive than previous studies, the *BeppoSAX* observation also included only a single dip episode.

Previous observations of X1624–490 have been limited either by the short duration of the observations or by the signal-to-noise ratio of the data; a thorough investigation requires a baseline of several orbits, coupled with a collecting area and efficiency large enough to study the spectral variability on short timescales. In this paper, we present light curves obtained with *RXTE* covering 4.5 contiguous orbits of

X1624–490, during which both strong dipping and strong flaring took place. We derive an accurate system ephemeris, and perform a detailed study of the spectral variability in dips. A companion paper will contain our analysis of the evolution and physics of the flares (Bałucińska-Church et al. 2000b, hereafter Paper II).

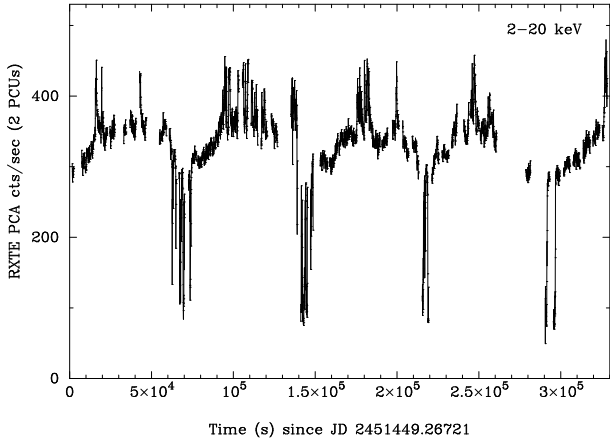


Fig. 1.— The X-ray light curve of X1624–490, 1999 September. The energy range covered is 2–20 keV, and the time binning is 64 sec.

2. Observations

We observed X1624–490 with *RXTE* (Bradt, Rothschild, & Swank, 1993) from 1999 September 27 18:22 UT – October 1 13:11 UT, for an on-source total good time of 212 ksec. The X-ray data presented here were obtained using the PCA instrument with the Standard 2 and Good Xenon configurations, with time resolutions of 16 sec and $< 1\mu\text{sec}$ respectively. The PCA consists of five Xe proportional counter units (PCUs) numbered PCUs 0 through 4, with a combined total effective area of about 6500 cm^2 (Jahoda et al 1996). Only PCUs 0 and 2 were reliably on throughout our observations, and we limit our analysis to data from these detectors. Data were also obtained with the HEXTE phoswich detectors, which are sensitive over the energy range 15–250 keV (Rothschild et al. 1998). However, because of the cut-off spectral shape of X1624–490, the counts detected were limited to energies < 25 keV, and the HEXTE data did not in this case provide any information additional to that gained using the PCA.

Based on a preliminary determination of the source ephemeris, derived from the above observations and the *RXTE* All Sky Monitor (ASM) light curve, we scheduled the balance of our *RXTE* pointed observing time to capture a complete dip episode, uninterrupted by Earth occultations and South Atlantic Anomaly passages. These observations were performed on 1999 November 12:20–16:21 UT, for a total good time of 14.3 ksec. For this observation, PCUs 0, 2, and 3 were reliably on throughout.

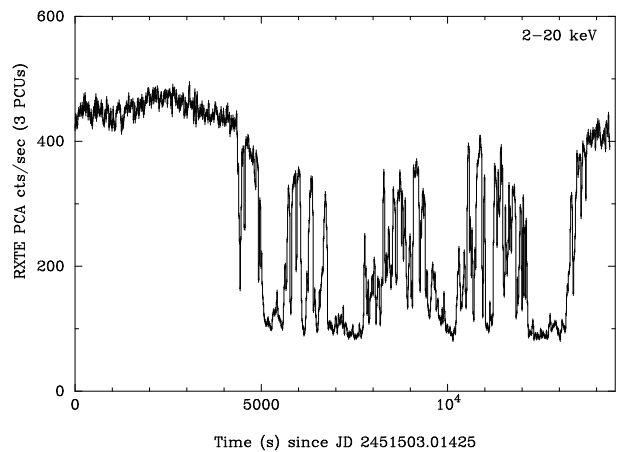


Fig. 2.— The 1999 November light curve in the 2–20 keV band, with 16 sec time resolution, showing the wealth of detail in a single dip episode from X1624–490.

We performed our data analysis using the *RXTE* standard analysis software, FTOOLS 5.0. Background subtraction of the PCA data was performed utilizing the “skyvle/skyactiv 20000131” models generated by the *RXTE* PCA team. The quality of the background subtraction was checked in two ways: (i) by comparing the source and background spectra and light curves at high energies (50–100 keV) where X1624–490 itself no longer contributes detectable events; and (ii) by using the same models to background-subtract the data obtained during slews to and from the source. We conclude that our background subtractions in the 2–20 keV energy range are accurate to a fraction of a count per second. Since one of our goals was a sensitive spectral analysis, we took pains to check the quality of both the background subtraction and the response matrices used, including a careful analysis of Crab calibration obser-

vations on 1999 September 26, October 13, November 8, and November 23, bracketing our observations of X1624–490. Based on this work, we added 2% systematic errors to the spectral fits.

Our orbital ephemeris calculations made use of two standard tools for establishing periodicities: a discrete Fourier transform technique optimized for unevenly-sampled time series (Scargle 1989), and a period-folding code utilizing the L-statistic (Davies 1990). Errors were calculated using the formulas intrinsic to these methods, and corroborated by fitting periodic functions to the unfolded light curve data and calculating the formal errors on the orbital period and epoch directly.

The search for fast variability in X1624–490 utilized the high time resolution PCA data obtained in the Good Xenon mode. Discrete power spectral density distributions (PSDs) were calculated by dividing the data into segments of uniform length, performing fast Fourier transforms of each, and averaging the results. The PSDs were normalized such that their integral gives the squared RMS fractional variability (Miyamoto et al 1991; van der Klis 1989). We subtracted the Poisson noise level from the power spectra, taking into account the modifications expected from PCA detector deadtime.

3. Results

3.1. Overall source behavior

In Figure 1, we show the background-subtracted 2–20 keV light curve for the 1999 September observation. Superimposed on the mean persistent flux levels, the most prominent features of the observation are four regular dips separated from each other by ~ 21 hrs, representing the orbital period of the system, and strong irregular flaring, most evident at phases $\phi=0.30$ –0.75 (assigning $\phi=0$ to the dip center). The 1999 November observation is shown in Figure 2, and provides a good illustration of the prodigious amount of detail in an individual dip from this source. The complex phenomenology seen in the overall light curve becomes more amenable to examination when we divide the 1999 September data into four energy bands covering 2–6, 6–10, 10–15, and 15–20 keV (Figure 3). (This is, incidentally, the first time the variability of the source above 10 keV has been accessible with good signal to noise.) From this Figure, we can come to the following qualitative conclusions:

- Dips are deepest at lower energies, but are still

(barely) discernable above 15 keV.

- The flaring is a higher-energy effect, not visible in the 2–6 keV range, but becoming the dominant feature in the 10–15 keV and 15–20 keV light curves. Examining light curves with even finer energy resolution, we can determine that flaring first becomes significant above 8 keV.

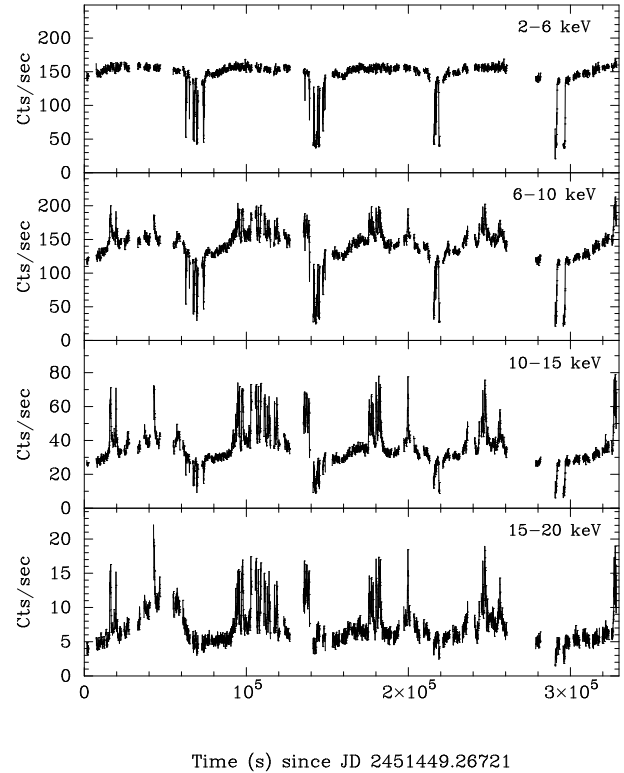


Fig. 3.— The X1624–490 light curve from 1999 September, broken down into several bands to show the energy dependence of the dipping and flaring activity.

3.2. The ephemeris of X1624–490

Applying the period search algorithms to the 1999 September PCA observation, we find a best-fitting period of 20.98 ± 0.14 hrs. This is consistent with previous estimates from datasets of limited duration, but for a useful long-term ephemeris, we turn to the publicly-available data from the *RXTE* ASM. The ASM (Levine et al. 1996) consists of three similar Scanning Shadow Cameras, sensitive to X-rays

in the 2–12 keV energy band, that cover \sim 80% of the sky every 90 minutes, with each datapoint representing a flux measurement from a single 90s dwell. X1624–490 is detected in the ASM with a weighted mean net count rate of 3.61 ± 0.01 count sec $^{-1}$. (For comparison, the Crab Nebula produces a count rate of \sim 75 ASM count sec $^{-1}$.) For this work, we analyzed data spanning the 1616 days from 1996 January 5 to 2000 June 8. The 21-hr orbital periodicity shows up strongly even in a rudimentary Fourier transform of the data at a frequency of $(1.3306 \pm 0.0002) \times 10^{-5}$ Hz. Combining Fourier and period folding analysis, we derive an orbital ephemeris for X1624–490 of

$$245\ 0088.63918(69) + N \times 0.869907(12) \text{ (JD).}$$

This orbital period (20.8778 ± 0.0003 hrs) is a two-significant-figure improvement over previous derivations, with a predictive value limited only by the phase jitter and irregularity of individual dips. It is sufficiently accurate to extend back to e.g. the EXOSAT observations of X1624–490 obtained in 1985 March 25–27, with no cycle-count ambiguity.

3.3. A QPO search

Recently, a new type of quasi-periodic oscillation (QPO) has been discovered in three of the dipping sources. The feature was first seen in X1323–619, where a \sim 1 Hz QPO was detected with an rms amplitude of 9%, remaining roughly constant in the persistent emission, the dips, and during the bursts (Jonker, van der Klis & Wijnands 1999). Similar features have been observed in X0748–676, with a central frequency ν that varied between 0.6 and 2.4 Hz and rms amplitudes of 8–12%, and in X1746–370, with $\nu=1.0\text{--}1.6$ Hz and rms amplitude 7% (Homan et al. 1999; Jonker et al. 2000). The QPO in X0748–676 are present in all the observations analyzed by Homan et al. (1999) except the pointing with the highest count-rate. For X1746–370 the picture is even more clear-cut; the atoll-source “island” and “banana” (Hasinger & van der Klis 1989) branches are well defined by the data, and the QPOs are absent during the latter.

For all three sources, there is little or no dependence of the QPO strength on the photon energy. This is very unusual: the amplitude of all other types of QPO seen in Z sources, atoll sources, and black hole candidates (BHC) from 0.01–1200 Hz shows a strong dependence on photon energy. Clearly the dipper QPO are a different phenomenon, related to the high source inclination, and perhaps linked directly

to the modulating effect of material in the accretion stream or at the disk edge; the exact mechanism is still open to conjecture. As this QPO is not observed in other LMXBs at lower inclinations, variations in the mass accretion rate are unlikely to be directly responsible, although the disappearance of the QPO at higher inferred mass accretion rates may be due to changes in the accretion geometry. The most likely candidate is some modulating effect caused by the accretion stream, or partial covering of an extended X-ray source by a near-opaque medium; this structure may disappear, change size, or change in optical depth at higher accretion rates.

We have searched the X1624–490 data for evidence of similar QPO activity, and find none. The extensive data set at our disposal allows us to place a rather stringent upper limit of 1% on the rms amplitude of a feature between 0.5–2 Hz with a FWHM of 0.4 Hz.

The absence of such features in X1624–490 is perhaps not surprising; 1 Hz QPOs are observed in XB1323–62 and XB1746–37 in the low-intensity island state of these atoll sources, but are not visible in the higher-intensity banana state. The derived hardness-intensity and color-color diagrams for the current observations of X1624–490 are dominated by the dip and flare activity and give no direct indication of which of the two states the source may be in, however the high overall source luminosity (see below) implies a high accretion rate, perhaps incompatible with the production of such QPO.

3.4. Spectral evolution during dipping

The energy bands in Figure 3 were chosen to emphasise and isolate the dipping activity, which dominates the light curve in the lowest band, and flaring, which dominates in the two bands above 10 keV. From Figures 2 and 3, it can be seen that there is a high degree of fast variability in dipping on timescales of \sim 32 s, and that there is a tendency for dipping to saturate at a constant low level. Moreover, the 2–6 keV light curve shows that dipping consists of two stages: deep dipping with associated rapid variability, preceded and followed by relatively shallow shoulders to the dipping which last \sim 12,000 s. Flaring, although apparently random in occurrence, is generally not observed during dip episodes at the high level seen outside dips. However, there appears to be a section of flaring data at $\sim 1.4 \times 10^5$ s, where the flaring coincides with the weak shoulder of the second dip.

We chose to study the spectral evolution through the dip episodes in the 1999 September observation in two stages. First, we accumulated spectra from a limited subset of the data, ruthlessly eliminating any data sections with even a suggestion of flare contamination. This approach produced 4 spectra, one for the non-dip emission, two at intermediate dipping levels, and a saturated dip spectrum. We fit these simultaneously using a wide range of models to allow elimination of most of these, and determine the probable form of the best-fit model. In the second stage, we divided the bulk of the observation into intensity bands and fit these jointly using the model determined from the first stage. This approach gave us confidence in our data selection criteria and enabled us to perform a sensitive search for subtle features.

3.4.1. Stage 1: Simultaneous fits to 4 spectra

Because of the strong spectral changes associated with flares, it was essential to avoid any possibility of data contamination with flare activity in our first pass. We thus selected data from the region around $\sim 1.7 \times 10^5$ s (in Figure 1), consisting of a complete satellite orbit of data during which no flaring is detected. A deep dip spectrum was obtained from that part of the third dip which reached a saturated, stable lower level in the low-energy light curve. All traces of dip ingress and egress were removed by selecting 320 seconds of data beginning at 2.1678×10^5 s from the start of the observation. Other dip spectra were selected in intensity bands at $180\text{--}190$ count s^{-1} and $130\text{--}140$ count s^{-1} . The total source counts contained in the 4 spectra selected, from non-dip to the deepest dipping respectively, were $\sim 7.4 \times 10^5$, 3.5×10^4 , 4.4×10^4 , and 2.2×10^4 .

These four spectra were first fitted simultaneously using simple, one-component models. In all cases, the parameters specifying the emission process such as the power law photon index were chained between the four spectra, since these cannot change during dipping. Results for all model fitting are shown in Table 1. (All values of the hydrogen column density quoted in the tables are in units of 10^{22} atoms cm^{-2} , and errors are quoted to 90% confidence.)

Simple models were unable to fit the spectra: an absorbed cut-off power law gave a χ^2 per degree of freedom (*dof*) of 8104/188; an absorbed bremsstrahlung model gave a χ^2/dof of 8789/189 and an absorbed blackbody model gave a χ^2/dof of 12666/189. Next, the two-component model consisting of a blackbody

plus cut-off power law was tried, first with the non-dip spectrum alone. A good fit was obtained with $\chi^2/\text{dof} = 20/46$, and so this model was applied to simultaneous fitting of all four spectra, producing an overall fit statistic of $\chi^2/\text{dof} = 231/180$. The two-component model has the form: $\text{AG}(\text{AB.BB} + \text{PCF.CPL})$, where AG represents Galactic absorption, BB the blackbody component, CPL the cut-off power law, AB additional absorption during dipping and PCF the progressive covering factor. This is the model shown to be able to describe spectral evolution in dipping in other LMXB dipping sources (see Introduction), and in this model the point-source blackbody is understood to be absorbed rapidly when the envelope of the absorber covers the neutron star, whereas the extended Comptonized emission is covered progressively as the absorber moves across the extended source.

Strong broad, residuals at ~ 6.4 keV were found, at the level of 4% in the non-dip spectrum, too high to be due to residual uncertainty in the instrument response function, and so a Gaussian line was included to the above model as a source term. Because of a tendency for widths of broad lines to increase in spectral fitting by absorption of continuum emission into the line, it was necessary to fix the width, and tests showed that 0.4 keV was appropriate. Fitting this model to 4 spectra simultaneously required the normalization of the line to decrease systematically in dipping, from 2.59×10^{-3} photon $\text{cm}^{-2} \text{ s}^{-1}$ in non-dip to 5.17×10^{-4} photon $\text{cm}^{-2} \text{ s}^{-1}$ in deep dipping. Fitting the deep dip with the latter normalization gave $\chi^2/\text{dof} = 38/45$, whereas fixing the normalization at the non-dip value gave $\chi^2/\text{dof} = 130/46$, demonstrating the significance of the decrease. Thus, we included the line within the progressive covering term to give a model: $\text{AG}(\text{AB.BB} + \text{PCF}(\text{CPL} + \text{GAU}))$. Using this approach, no change in the line normalization was necessary, showing that the line was well modeled by assuming that it originates in the same region as the Comptonized emission, i.e. the ADC, and so is subject to the same covering factor.

At this stage, the fits still exhibited excesses at low energy, resulting in a quality of fit that was still not acceptable. Consequently, we next added the same interstellar dust scattering terms to the spectral model that were used in the *BeppoSAX* study (see Bałucińska-Church et al. 2000a, and above), including terms both for scattering out of the beam and into the beam, giving the final form of the fitted model:

$$\text{AG } e^{-\tau} (\text{AB . BB} + \text{PCF (CPL + GAU)}) + \\ \text{AG } (1 - e^{-\tau}) (\text{BB} + \text{CPL} + \text{GAU}).$$

The factor $e^{-\tau}$ represents scattering out of the beam, while the $(1 - e^{-\tau})$ term is scattering into the beam. For non-dip emission, we make the usual assumption that the intensities of these components are equal (e.g. Martin 1970). (Non-standard spectral components $e^{-\tau}$ and $(1 - e^{-\tau})$ were produced for inclusion in spectral fitting with the XSPEC package.) With the addition of the dust scattering terms, the low energy excesses in the spectra were removed and a good fit obtained to all 4 spectra simultaneously with a $\chi^2/dof = 127/179$.

While our fitted model may appear over-constrained at first sight, it is crucial to note that in our simultaneous fits, *all* emission terms (blackbody kT and normalization, Γ , cutoff and normalization values) are fixed at their non-dip values, and the dust scattering parameters are fixed at their SAX MEC values. Only the column densities and covering fraction are free parameters, in a joint fit to 4 spectra of differing shapes and over a fivefold range of intensities.

In addition, to demonstrate that the inclusion of the line and dust scattering do not favor the two-component model over the other candidate models, the same terms were added to the one-component models fits in the most favorable way, i.e. with the line being subject to progressive covering to account for its variation in intensity during dipping. The results of fitting all models are included in Table 1. It can be seen that adding the line and dust scattering to simple models results in some improvement, but the fits are still unacceptable. Although the overall fit of the best-fit model to the 4 spectra was acceptable, the spectra (non-dip to deepest dip) having individual values of χ^2/dof of 20/46, 74/46, 60/46 and 38/46, the intermediate dip spectra had broad excesses at ~ 5 keV. This was investigated further in our next step, which was to analyze spectra from the whole observation, with much improved statistics at the intermediate levels.

3.4.2. Stage 2: Spectra from the complete observation

Spectra were selected in intensity bands 20 count s^{-1} wide, with a non-dip spectrum taken from the band 300–320 count s^{-1} . Five dip spectra were accumulated corresponding to intensity bands: 280–300, 260–280, 220–240, 100–120 and 60–80 count s^{-1} , such that the

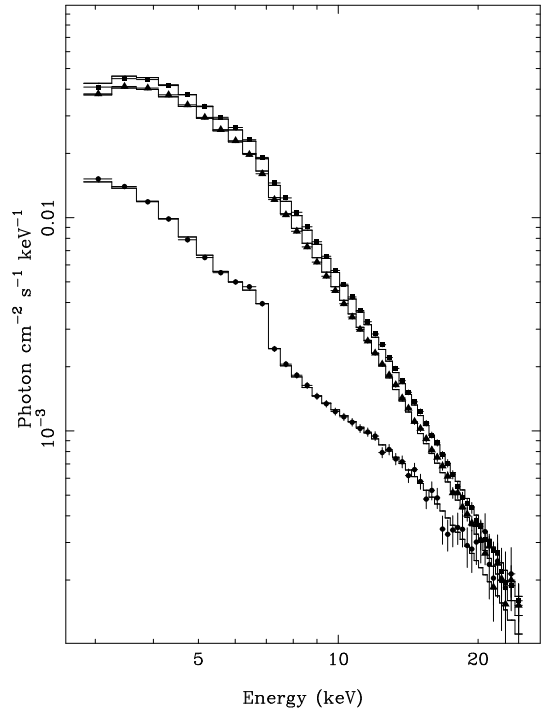


Fig. 4.— Spectral fits to the non-dip spectrum (squares); the intermediate dip level (260–280 count s^{-1}) representing the deepest level in the shoulders of dipping (see text - triangles); and the deepest dip spectra (circles).

non-dip spectrum plus the first two of these provide good coverage of the shoulders of dipping, and the remaining spectra span the main, deeper parts of dips. We excluded a section of data 60 ksec in length at the beginning of the observation, in which the 15–20 keV light curve (Figure 3) shows unusual behavior. The six spectra thus derived have a considerably higher total count rate than the 4 spectra previously used, allowing the relatively small intensity changes in the shoulders of dipping to be investigated. We applied our best fit model first to these shoulders.

In Figure 4, the unfolded spectrum of the non-dip level, the deepest spectrum in the shoulders of dipping, and the deepest dip spectrum of all are shown. The dip shoulder spectrum can be approximately fitted as a constant vertical shift downwards of the non-dip spectrum, indicating that electron scattering is the dominant absorption process, and that photoelectric absorption is negligible. From the fitting it is

also clear that the blackbody requires zero column density, for all spectra in the shoulders of dipping. Thus, the intensity reduction in the shoulders must correspond to the absorber overlapping the extended ADC but not the neutron star, and the outer regions of the absorber which are involved in this overlap must be highly ionized. Comparison of the non-dip and deepest-dip spectra also reveals a vertical shift between the spectra at 20 keV showing the effects of electron scattering. This effect, clear in intensity-selected data with good statistics, was not visible in Stage 1. Consequently, it becomes necessary to upgrade the PCF model previously used to a progressive covering model in which X-rays are attenuated by two processes: electron scattering and possible photoelectric absorption expressed in the form:

$$(f e^{-N_e \sigma_T} e^{-N_H \sigma_{PE}} + (1 - f))$$

where N_e is the electron column density, σ_T is the Thomson cross-section, and σ_{PE} the photoelectric cross-section, and the contributions of scattering and absorption are allowed to be independent.

Good fits were obtained with this model, as shown in Figures 5 and 6. The emission parameters used are shown in Table 2, and we present the parameters of the best fits to the complete set of intensity-selected spectra in Table 3. The values of the emission parameters used for the complete set agree well within the errors with the values shown for the best-fit model of Table 1.

Initially the fit to the intermediate dip spectrum at $220-240 \text{ c s}^{-1}$ was relatively poor with an excess seen in the spectrum at $\sim 5 \text{ keV}$ and $\chi^2/\text{dof} = 145/45$. This spectrum was investigated further. A concern throughout this work was the possibility of dip spectra being contaminated by flaring, given the strong spectral changes we show take place in flaring in Paper II. Deep dip spectra will not be contaminated as flaring is associated with the neutron star, but we cannot rule out the possibility for the intermediate spectra may be. However, it appears that this excess has another cause. If the absorber is highly ionized, residual photoelectric absorption will be due to the ionized absorber, not neutral absorption. In the early stages of dipping, this is not a problem since attenuation of the Comptonized ADC emission is caused by the large electron column density N_e^{CPL} whereas the absorption column N_H^{CPL} remains zero (Table 3) until dipping becomes deep. In deep dipping, a

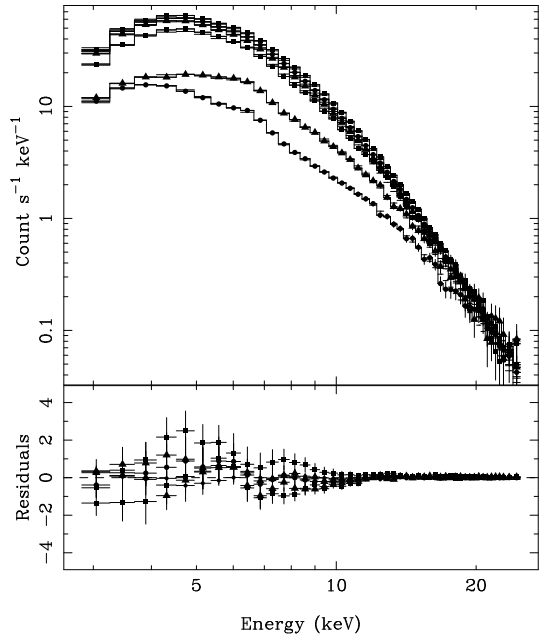


Fig. 5.— Simultaneous fits to the non-dip and five dip spectra from the complete 1999 September observation, using a two-component model consisting of a point-like blackbody and progressive covering of an extended Comptonized region, plus a halo and line (see text for details). Data and residuals for each input spectrum are marked as follows for easier visual identification: non-dip - squares; spectra of progressively deeper dipping: circles, triangles, squares, circles and triangles.

combination of neutral absorber and electron scattering provides satisfactory fits, as could be expected since the degree of ionization must decrease inside the absorber. Similarly, in shallow dipping the blackbody is not absorbed, and in deep dipping totally absorbed, so the question of ionized absorber does not arise. The exception is the intermediate spectrum with $N_H^{BB} = 20 \times 10^{22} \text{ atom cm}^{-2}$ (Table 3). Refitting this spectrum with an ionized absorber for the blackbody resulted in a much-improved fit with $\chi^2/\text{dof} = 53/44$ (as shown in the Table), and a value of $\xi = 118$ for the ionization parameter. Strictly speaking, even this model is not totally satisfactory since the ‘*absor*’ model of XSPEC that was used is based on a power law source whereas X1624–490 is dominated by blackbody emission. However, we believe we

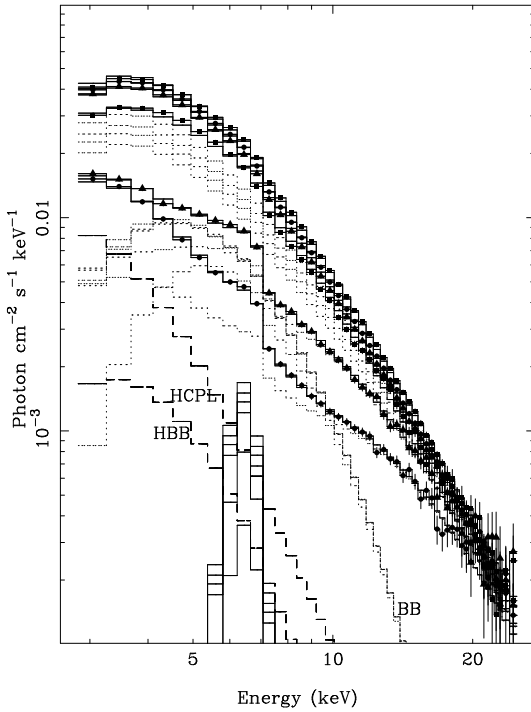


Fig. 6.— The unfolded spectra for the fits shown in Figure 5, showing the contributions of the blackbody (BB), halo, and line to the overall fits. The halo components (scattered into the beam) are HBB and HCPL for the blackbody and cut-off power law contributions; the line halo is included but cannot be seen on this scale.

are now at the limit of what can usefully be learned through spectral fitting, and further refinements will produce diminishing returns.

4. Discussion

We have shown that spectral evolution during dipping in X1624–490 is well-described by a combination of the point-source blackbody plus extended Comptonization emission model, with a “progressive covering” treatment of the absorption process. To this basic model it was necessary to add a broad Gaussian line at ~ 6.4 keV, and terms to describe interstellar dust scattering both out of and into the line-of-sight. The blackbody temperature kT , and power law index Γ , and cut-off energy E_{CO} from these *RXTE* fits (Table 2) are in good agreement with the values determined from the *BeppoSAX* fitting, of kT

$= 1.37 \pm 0.07$ keV, $\Gamma = 2.0_{-0.7}^{+0.5}$ and $E_{CO} \sim 12$ keV (Balucińska-Church et al. 2000a). During the *RXTE* observations, the total luminosity in the 1–30 keV band was 1.47×10^{38} erg s $^{-1}$ at a distance of 15 kpc (Christian & Swank, 1997), approximately twice that seen during the *BeppoSAX* observation, and thus complete consistency of emission parameters should not necessarily be expected. The bolometric blackbody luminosity was 2.3×10^{37} erg s $^{-1}$, or 15% of the total luminosity, smaller than the 36% measured by *BeppoSAX* (Balucińska-Church et al. 2000a). Luminosity considerations are discussed further in Paper II.

In dipping, the blackbody component is rapidly and completely removed once the neutron star is covered. The clear occurrence of saturated dipping in most of the dips observed indicates that in addition to the removal of the blackbody, absorption of the Comptonized emission also reaches a stable level. This must be due either to an absorber of smaller angular extent than the ADC by a fixed fraction, or to the presence of blobs within the absorber envelope such that $\sim 20\%$ of the absorber is transmitting in less dense regions in between blobs of higher density. The Gaussian line varied in dipping in a way that could be described by giving it the same covering factor as the ADC. There are two contributions to the excess at low energies: the dust-scattered halo components which are shown separately in Figure 6, and also the part of the extended Comptonized emission that is not covered at any level of dipping. Table 3 shows the covering fraction rising to a maximum value of $\sim 80\%$ in the best-fit model, unlike other dipping sources such as XB1916–053 (Church et al. 1997) where dipping reaches a depth of 100% at all energies below 10 keV and the covering fraction similarly reaches 100%, proving that the angular extent of all emission regions is less than that of the absorber. In the present case, there may be two reasons why this does not happen: either the absorber is somewhat smaller in angular extent than the ADC extended emission, or more likely, the absorber in the outer accretion disk is not uniformly dense within its envelope, but blobby, as indicated by the strong variability within dipping. We investigate this possibility further below.

We can obtain further information on the ADC from the duration of dip ingress and egress. The sharp ingress to deep dipping, and the fast variability within dipping, take place on timescales of ~ 32 s, and this is

clearly associated with absorption of the point-source blackbody component. However, the long, shallow shoulders of the dips map a gradual process of dip ingress and egress which is consistent with the extended ADC being covered by relatively less dense absorber before the absorber envelope reaches and obscures the neutron star. The duration of the ingress shoulder is $\sim 12 \pm 2$ ks from the present observation, and we can also derive a duration of $\sim 13 \pm 2$ ks from studying the EXOSAT light curve (Church & Bałucińska-Church 1995). Some asymmetry can be seen in the shoulders, and we use the shorter ingress time corresponding to the leading edge of the bulge on the accretion disk, not the trailing edge, which would give a longer shoulder depending on the absorber dimensions rather than the dimensions of the ADC. For an absorber of larger angular extent than the ADC, the ingress time Δt is the time taken by the leading edge to cross the ADC given by the velocity of material in the outer disk:

$$2\pi r_{\text{disk}}/P = d_{\text{ADC}}/\Delta t,$$

where r_{disk} is the disk radius, P is the orbital period and d_{ADC} is the diameter of the ADC. In the event that the absorber has somewhat smaller angular extent than the ADC, as is a possible interpretation of spectral fitting, the ingress time gives the diameter of the absorber, and the source region could be as much as 20% larger. Using a period of 20.87 hr from our ephemeris work above, and a mass of $1.4M_{\odot}$, a value of 1.0×10^{11} cm can be calculated for the accretion disk radius (Frank et al. 1987). Using our observed Δt , we derive from this an ADC radius of 5.0×10^{10} cm. The average ingress time from the EXOSAT and *RXTE* data gives 5.3×10^{10} cm. If the absorber has smaller angular size than the ADC, then the above calculation provides the absorber radius, so that the ADC could be up to 20% larger than this, on the basis of the covering fraction only reaching $\sim 80\%$ in deepest dipping.

We can use the above radius of the ADC to make some comparisons with simple ADC theory. The maximum radius of an ADC that can be supported in hydrostatic equilibrium r_{eq} is given by the condition that $kT < GM_x m / r_{\text{eq}}$ where M_x is the mass of the neutron star and m the mass of a proton. This provides a simple formula:

$$r_{\text{eq}} \simeq \frac{1.6 \times 10^{11} M_x}{T_{\text{ADC}} M_{\odot}} \text{ (cm)}$$

where T_{ADC} is the temperature of the ADC in units of 10^7 K. We can use the Comptonization cut-off energy E_{CO} obtained in the present analysis of 12 keV to place limits on the electron temperature kT_e of 4–12 keV, corresponding to an optical depth to electron scattering $\tau < 1$ or $\tau > 1$ respectively. For low optical depth, $kT_e \sim E_{CO}$, but for higher optical depth, even if Comptonization is not saturated, kT_e will be a factor of 2.5–3.0 smaller than E_{CO} (e.g. Dove et al. 1997). Using these limits on electron temperature, we find $r_{\text{eq}} = 1.6 - 5.3 \times 10^{10}$ cm, the smaller value corresponding to the higher temperature. Comparing these with $r_{\text{ADC}} \sim 5 \times 10^{10}$ cm from our dip ingress calculation, we can see that there is better agreement with r_{eq} calculated assuming a higher optical depth to electron scattering. We thus have evidence that the ADC is maintained in hydrostatic equilibrium. The ADC is likely to be “thin”, with a height-to-radius ratio of the order of 10% at its outer edge, as opposed to being spherical. For example, for an ADC radius of 5×10^{10} cm, it is unlikely that the absorber on the outer disk would be able to cover a spherical ADC extending to this distance in the vertical direction.

This paper utilizes *RXTE* All Sky Monitor results made publicly available by the ASM/*RXTE* Team, including members at MIT and NASA/Goddard Space Flight Center, and also archival data obtained through the High Energy Astrophysics Science Archive Research Center Online Service, also at NASA/GSFC.

REFERENCES

Angelini, L., Parmar, A.N., White, N.E., 1997, Proc. IAU Colloquium 163, Eds. D.T. Wickramasinghe, G.V. Bicknell, L. Ferrario
 Bałucińska-Church, M., Church, M.J., Oosterbroek, T., Segreto, A., Morley, R., & Parmar, A.N., 1999, A&A, 349, 495
 Bałucińska-Church, M., Humphrey, P.J., Church, M.J, & Parmar, A.N., 2000a, A&A in press
 Bałucińska-Church, M., Barnard, R., Church, M.J, & Smale, A.P., 2000b, ApJ in preparation.
 Bradt, H.V., Rothschild, R.E., & Swank, J.H., 1993, A&AS, 97, 355
 Christian, D.J., & Swank, J.H., 1997, ApJS, 109, 177
 Church, M.J., & Bałucińska-Church, M., 1995, A&A, 300, 441

Church, M.J., Dotani, T., Bałucińska-Church, M., Mitsuda, K., Takahashi, T., Inoue, H., & Yoshida, K., 1997, *ApJ*, 491, 388

Courvoisier, T.J.-L., Parmar, A.N., Peacock, A., & Pakull, M., 1986, *ApJ*, 309, 265

Davies, S.R., 1990, *MNRAS*, 244, 93

Dove J. B., Wilms J., Maisack M., & Begelman M. C., 1997, *ApJ*, 487, 759

Frank, J., King, A.R., & Lasota, J.-P., 1987, *A&A*, 178, 137

Hasinger, G., & van der Klis, M., 1989, *A&A*, 225, 79

Homan, J., Jonker, P.G., Wijnands, R., van der Klis, M., & van Paradijs, J., 1999, *ApJ*, 516, L91

Jahoda, K., Swank, J. H., Giles, A. B., Stark, M. J., Strohmayer, T., Zhang, W., & Morgan, E. H., 1996, in *EUV, X-ray and Gamma-Ray Instrumentation for Astronomy VII*, ed O. H. Siegmund (Bellingham, WA: SPIE), 59

Jones M.H., & Watson M.G., 1989, Proc. 23rd EELAB Symposium, ESA SP-296, p. 439

Jonker, P.G., van der Klis, M., Homan, J., Wijnands, R., van Paradijs, J., Méndez, M., Kuulkers, E., & Ford, Eric C., 2000, *ApJ*, 531, 453

Jonker, P.G., van der Klis, M., & Wijnands, R., 1999, *ApJ*, 511, L41

Levine, A.M., Bradt, H., Cui, W., Jernigan, J.G., Morgan, E.H., Remillard, R., Shirey, R.E., & Smith, D.A., 1996, *ApJ*, 469, L33

Martin, P.G., 1970, *MNRAS* 149, 221

Miyamoto, S., Kimura, K., Kitamoto, S., Dotani, T., & Ebisawa, K., 1991, *ApJ*, 383, 784

Parmar, A.N., White, N.E., Giommi, P., & Gottwald, M., 1986, *ApJ*, 308, 199

Rothschild, R. E., Blanco, P. R., Gruber, D. E., Heindl, W. A., MacDonald, D. R., Marsden, D. C., Pelling, M. R., & Wayne, L. R., 1998, *ApJ*, 496, 538

Scargle, J.D., 1989, *ApJ*, 343, 874

Smale, A.P., Mason, K.O., White, N.E., & Gottwald, M., 1988, *MNRAS*, 232, 647

Smale, A.P., Mukai, K., Williams, O.R., Jones, M.H. & Corbet, R.H.D., 1992, *ApJ*, 400, 330

van der Klis, M., 1989, in *Timing Neutron Stars*, H. Ogelman & E.P.J. van den Heuvel (eds), Cambridge University Press, p. 252

Watson, M.G., Willingale, R., King, A.R., Grindlay, J.E., & Halpern, J., 1985, *Space Sci Rev.*, 40, 195

White, N.E., & Swank, J.H., 1982, *ApJ*, 253, L61

This 2-column preprint was prepared with the AAS *LATeX* macros v4.0.

TABLE 1

RESULTS FROM SIMULTANEOUS FITS TO THE NON-DIP SPECTRUM AND 3 DIP SPECTRA.

Model	N_H	kT (keV)	Γ	χ^2/dof
Blackbody	$0.0^{+0.1}_{-0.0}$	1.57 ± 0.01	...	12666/189
Bremsstrahlung	4.48 ± 0.26	4.79 ± 0.60	...	8789/189
Cut-off power law	$12.5^{+1.1}_{-0.3}$...	$3.31^{+0.19}_{-0.06}$	8104/188
Two-cpt (prog. cov.)	11.6 ± 0.7	1.55 ± 0.04	3.00 ± 0.14	231/180
Blackbody, line, dust	$0.0^{+0.1}_{-0.0}$	1.56 ± 0.01	...	6677/182
Bremsstrahlung, line, dust	6.0 ± 0.1	4.46 ± 0.10	...	3433/182
Cut-off power law, line, dust	12.5 ± 0.1	...	2.99 ± 0.12	2810/181
Two-cpt, line, dust (prog. cov.)	10.1 ± 0.8	1.52 ± 0.05	2.74 ± 0.17	127/179

TABLE 2

BEST-FITTING MODEL TO THE NON-DIP SPECTRUM

N_H	kT	Γ	E_{CO}	E_{line}
8.6 ± 3.1	1.32 ± 0.17	$2.29^{+0.66}_{-1.10}$	~ 12	$6.4^{+0.19}_{-0.49}$

TABLE 3

BEST FITS TO THE SIX SPECTRA

Spectrum	N_H^{BB}	N_H^{CPL}	N_e^{CPL}	f	χ^2/dof
Non-dip	8.6 ± 3.1	8.6 ± 3.1	0.0	0.0	54/45
$280-300 \text{ c s}^{-1}$	8.6 ± 3.1	$8.6^{+77}_{-3.1}$	286^{+89}_{-59}	0.123 ± 0.009	19/45
$260-280 \text{ c s}^{-1}$	8.6 ± 3.1	$8.6^{+3.4}_{-3.1}$	148 ± 10	0.300 ± 0.012	63/45
$220-240 \text{ c s}^{-1}$	23^{+15}_{-12}	$8.6^{+3.2}_{-3.1}$	120 ± 6	0.504 ± 0.005	53/44
$100-120 \text{ c s}^{-1}$	$> 10^3$	51 ± 2	53 ± 3	0.793 ± 0.006	44/45
$80-100 \text{ c s}^{-1}$	$> 10^3$	154 ± 5	60 ± 6	0.828 ± 0.006	28/45